ISSN (Print) 1226-1750
ISSN (Online) 2233-6656
Journal of Magnetics 31(2), 232-239 (2026) https://doi.org/10.4283/JMAG.2026.31.2.232

Deep Image Prior-Based Restoration with Spatial Resolution Enhancement and Noise Reduction in Mouse Cardiac Magnetic Resonance Imaging

Ji-Youn Kim[1], Hyuk-Jae Edward Kwon[2], and Kyoung-Nam Kim[3]*

[1]*Department of Dental Hygiene, Gachon University, 191, Hambangmoe-ro, Yeonsu-gu, Incheon 21936, Republic of Korea*
[2]*Department of Oral Biology, School of Dental Medicine, University at Buffalo, The State University of New York, Buffalo, NY 14214, USA*
[3]*Department of Biomedical Engineering, Gachon University, 1342, Seongnam-daero, Sujeong-gu, Seongnam-si, Gyeonggi-do 13120, Republic of Korea*

(Received 28 April 2026, Received in final form 16 June 2026, Accepted 16 June 2026)

Cardiac magnetic resonance imaging (MRI) in small animals is a powerful, non-invasive modality for assessing cardiac structure and function. However, acquiring high-quality images is challenging due to the small heart size and rapid heart rate in mouse models. In this study, we propose a deep image prior (DIP)-based image enhancement algorithm and evaluate its feasibility for four-dimensional (4D) mouse cardiac MR images. The proposed algorithm was modeled using a hybrid stopping strategy. Compared with the conventional approach combining block-matching and 4D filtering with total generalized variation, the proposed approach demonstrated improvements of 31.63%, 146.77%, and 63.16% in contrast-to-noise ratio, gradient magnitude, and perceptual sharpness index, respectively. In conclusion, the proposed DIP-based restoration framework with a hybrid stopping strategy shows potential for improving image quality in small-animal cardiac MRI by jointly reducing noise, mitigating blur, and enhancing apparent spatial resolution under an explicitly defined degradation model.

Keywords : cardiac magnetic resonance imaging, deep image prior, hybrid stopping strategy, super-resolution, noise reduction, quantitative evaluation of image quality

1. Introduction

Cardiac magnetic resonance imaging (MRI) is a representative diagnostic modality that enables the non-invasive and non-destructive evaluation of cardiac structure and function [1, 2]. Currently, it is widely regarded as the reference standard for the quantitative assessment of cardiac chamber volumes and systolic function [3]. In research settings, cardiac MRI is extensively used to study cardiovascular disease in small animal models, particularly mice, which are highly valuable for modeling human pathophysiology [4]. However, the small size of the mouse heart and its rapid heart rate present substantial technical challenges for acquiring high-resolution MR images [5]. These limitations result in a low signal-to-noise ratio and restricted spatial resolution, thereby reducing the accuracy of quantitative analyses.

Accurate characterization of mouse cardiac structure requires high-resolution MRI, which typically entails prolonged acquisition times. Such extended scans increase susceptibility to motion artifacts and reduce experimental efficiency [6,7]. Consequently, super-resolution and noise reduction techniques are essential for enhancing low-resolution, high-noise images acquired under constrained conditions. Conventional image enhancement approaches—including interpolation-based methods [8], compressed sensing (CS) [9], and supervised learning techniques using convolutional neural networks (CNNs) [10]—have been proposed. When applied to MRI, interpolation-based methods and compressed sensing (CS) approaches are limited in their ability to restore lost high-frequency information and may suffer from oversmoothing effects or residual reconstruction artifacts, potentially compromising image quality and structural fidelity. In addition, supervised learning technique and CNN either depend on large

*Corresponding author: Tel: +82-31-750-2615,
Fax: +82-31-750-8889
e-mail: kyoungnam.kim@gachon.ac.kr (Kyoung-Nam Kim)

volumes of paired training data or exhibit limited generalizability due to discrepancies between training and real-world data distributions.

Deep image prior (DIP)-based approaches have recently gained attention as a data-efficient alternative for medical image restoration and reconstruction because they exploit the implicit bias of randomly initialized convolutional networks without requiring large external training datasets [11, 12]. In MRI, DIP-related methods have been explored for reconstruction from incomplete or degraded measurements, including dynamic MRI applications in which temporal information is incorporated into the reconstruction process [13]. These studies demonstrated that untrained or self-supervised neural representations can provide useful regularization for ill-posed MRI reconstruction problems. However, most previous studies have focused primarily on reconstruction from undersampled measurements or on dynamic MRI reconstruction in larger anatomical settings, whereas small-animal cardiac MRI presents a distinct challenge due to the combination of small cardiac structures, rapid motion, limited SNR, and the need to preserve fine anatomical boundaries across cine frames [14]. The present study extends prior DIP-based and self-supervised MRI reconstruction approaches to four dimensional (4D) mouse cardiac MRI by treating the task as model-based restoration rather than conventional supervised super-resolution. The proposed framework jointly incorporates downsampling consistency, spatial regularization, temporal coherence, edge preservation, and hybrid convergence-based stopping to enhance apparent spatial resolution while suppressing noise and blur. Thus, the main contribution is the adaptation of DIP into a practical self-supervised restoration framework for small-animal 4D cine cardiac MRI.

In this study, we propose a DIP-based framework for simultaneous super-resolution and noise reduction, applied to 4D mouse cardiac MRI. The proposed method reconstructs high-resolution images from a single low-resolution input using a hybrid stopping strategy while effectively suppressing MRI-specific noise. By leveraging the structural properties of DIP, the framework aims to mitigate overfitting and preserve fine anatomical details of cardiac structures.

2. Materials and Methods

2.1. 4D cine MRI dataset

A publicly available preclinical mouse cardiac MRI dataset was utilized to evaluate the performance of the proposed DIP-based reconstruction framework. The dataset was originally introduced as an open-source resource for cardiac image segmentation and includes comprehensive cine short-axis MRI data with corresponding expert annotations [15].

All MRI data were acquired using a 9.4 T small-animal MRI system (Agilent Technologies, Santa Clara, CA, USA) equipped with high-performance gradient coils (up to 1,000 mT/m) and a 39 mm volume radiofrequency coil. For each mouse, a complete short-axis cine stack covering the left ventricle was acquired using approximately 8–11 contiguous slices with a slice thickness of 1.0 mm. The in-plane acquisition matrix was 128 × 128, and an interpolation factor of 2.0 yielded a reconstructed spatial resolution of approximately 0.1 × 0.1 mm². Additional imaging parameters included a repetition time of 5.0 ms, an echo time of 1.2 ms, and a flip angle of approximately 16°. The temporal resolution was 5.0 ms, resulting in 17–36 cardiac phases per cardiac cycle, depending on heart rate. Overall, the dataset contains 26,230 two-dimensional images derived from full cine acquisitions across all mice. Each image corresponds to a specific slice and cardiac timeframe, thereby forming a 4D dataset with spatial and temporal dimensions.

2.2. Deep image prior-based 4D MRI restoration with hybrid stopping strategy

Figure 1 illustrates the proposed self-supervised reconstruction framework based on DIP for simultaneous super-resolution and denoising of 4D MRI data. The degraded observation $\mathbb{Y} \in \mathbb{R}^{H \times W \times X \times T}$ is modeled as [16, 17]:

$$\mathbb{Y} = \mathcal{H}(\mathbb{X}) + \mathbb{N}, \tag{1}$$

where $\mathcal{H}(\cdot)$ denotes a degradation operator consisting of downsampling (factor = 2), and $\mathbb{N} \sim \mathcal{N}(0, \sigma_n^2)$ represents additive Gaussian noise with $\sigma_n = 0.05$. In this study, the term super-resolution is used in a model-based sense. The proposed network estimates a high-resolution 4D MRI volume whose degraded projection, obtained through the predefined operator $\mathcal{H}$, remains consistent with the observed low-resolution and noisy input. Therefore, the proposed framework should be regarded as a DIP-based restoration method that combines spatial resolution enhancement, denoising, deblurring, and temporal regularization. It does not imply unconstrained recovery of all high-frequency information lost during acquisition; rather, the recovered structures are those supported by the assumed forward degradation model, the implicit bias of the DIP network, and the imposed spatial–temporal regularization terms. The reconstructed 4D MRI $\hat{\mathbb{X}}$ is obtained by optimizing a randomly initialized CNN $f_\theta(\mathbb{Z})$, where $\mathbb{Z} \sim \mathcal{U}(0,1)$ is a fixed input tensor, such that $\hat{\mathbb{X}} =$

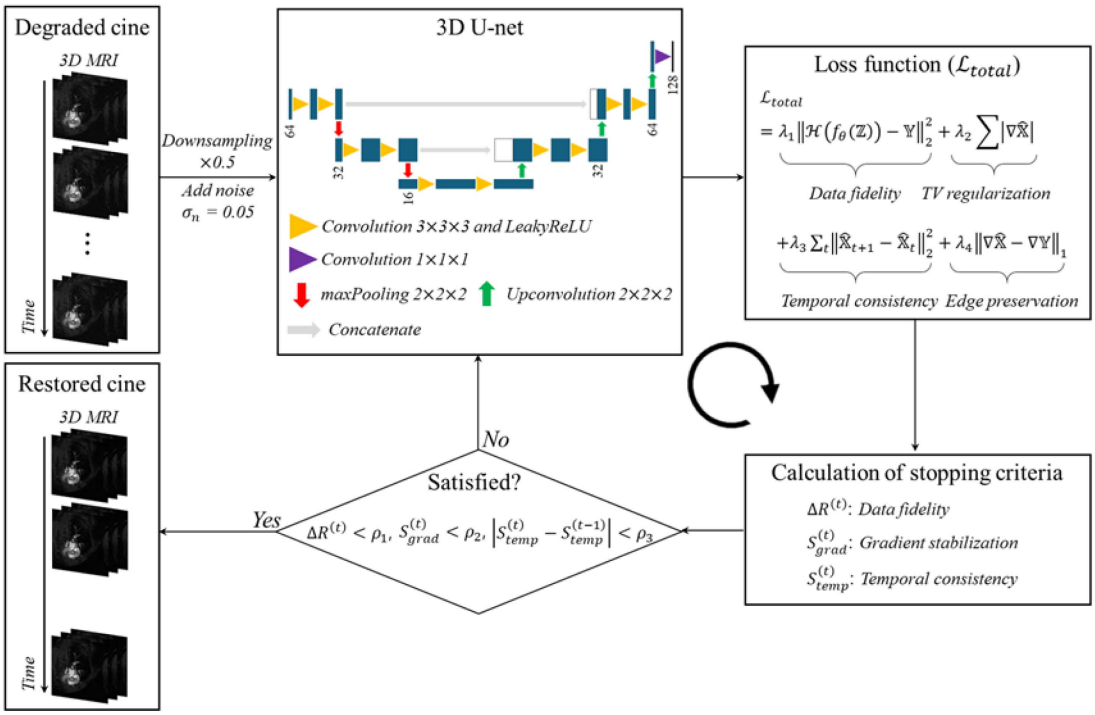

Fig. 1. (Color online) Overall flowchart of the proposed deep image prior (DIP)-based four-dimensional (4D) magnetic resonance imaging (MRI) restoration framework with a hybrid stopping strategy. The iterative process continues until all stopping conditions are satisfied, yielding the final restored 4D cine MRI with enhanced spatial resolution and reduced noise.

$f_\theta(\mathbb{Z})$. The network adopts a three-dimensional (3D) U-Net–like encoder–decoder architecture [18]. The network takes a low-resolution cine MRI volume as input and processes it through a three-level hierarchical structure composed of convolutional encoding, bottleneck representation, and symmetric decoding stages. In the encoder path, the input volume is progressively downsampled to extract high-level feature representations. Each encoding block consists of two consecutive 3D convolutional layers with kernel size 3 × 3 × 3, followed by LeakyReLU activation. Spatial resolution is reduced using max-pooling operations with a stride of 2 × 2 × 2, enabling the network to increase its receptive field while preserving contextual information. The number of feature channels is gradually increased across the encoder levels (e.g., 8, 16, 32, and 64 channels), enabling the network to learn increasingly abstract representations. In the decoder path, feature maps are progressively upsampled using transposed convolution (upconvolution) layers with a stride of 2 × 2 × 2. At each decoding level, the upsampled feature maps are concatenated with the corresponding encoder features via skip connections. This skip connection mechanism enables the network to preserve fine spatial details while recovering high-resolution structures. Each decoding block also consists of two 3D convolutional layers with LeakyReLU activation, with a gradual reduction in the number of feature channels. Finally, a 1 × 1 × 1 convolutional layer is applied to map the reconstructed feature representation to the output image space. The network is designed to generate a high-resolution 4D MRI volume, where spatial resolution is enhanced while maintaining temporal consistency across cine frames. The parameters θ are optimized using the Adam optimizer (learning rate = 1×10^{-3}, $\beta_1 = 0.9$, $\beta_2 = 0.999$) for up to 1,500 iterations. To simultaneously achieve super-resolution and denoising, the total loss function is defined as:

$$\mathcal{L}_{total} = \lambda_1 \|\mathcal{H}(f_\theta(\mathbb{Z})) - \mathbb{Y}\|_2^2 + \lambda_2 \Sigma |\nabla \hat{\mathbb{X}}| + \lambda_3 \Sigma_t \|\hat{\mathbb{X}}_{t+1} - \hat{\mathbb{X}}_t\|_2^2 + \lambda_4 \|\nabla \hat{\mathbb{X}} - \nabla \mathbb{Y}\|_1, \quad (2)$$

where $\lambda_1 = 1.0$, $\lambda_2 = 1 \times 10^{-5}$, $\lambda_3 = 5 \times 10^{-3}$, and $\lambda_4 = 1 \times 10^{-2}$. The first term enforces consistency with the degraded observation and implicitly enables inversion of the degradation operator for super-resolution. The second term suppresses noise via spatial total variation regularization [19]. The third term enforces temporal coherence across cine frames, and the fourth term preserves edge structures, thereby enhancing high-frequency anatomical details. Unlike conventional DIP approaches that rely on

frequency-based early stopping—which may prematurely suppress meaningful high-frequency components in super-resolution tasks—we propose a hybrid stopping strategy that jointly accounts for reconstruction fidelity, structural stabilization, and temporal consistency. Specifically, the normalized data fidelity residual is defined as:

$$R^{(t)} = \frac{\left\| \mathcal{H}(\mathbb{X}^{(t)}) - \mathbb{Y} \right\|_2^2}{\left\| \mathbb{Y} \right\|_2^2}, \tag{3}$$

with its variation given as $\Delta R^{(t)} = |R^{(t)} - R^{(t-1)}|$. The gradient stabilization term is defined as:

$$S_{grad}^{(t)} = \frac{\left\| \nabla \mathbb{X}^{(t)} - \nabla \mathbb{X}^{(t-1)} \right\|_2^2}{\left\| \nabla \mathbb{X}^{(t-1)} \right\|_2 + \varepsilon}, \tag{4}$$

where ε is set to 10^{-8}. The temporal consistency variation is defined as [20, 21]:

$$S_{temp}^{(t)} = \frac{1}{T-1} \Sigma_{m=1}^{T-1} \frac{\left\| \mathbb{X}_{m+1}^{(t)} - \mathbb{X}_m^{(t)} \right\|_2}{\left\| \mathbb{X}_m^{(t)} \right\|_2 + \varepsilon}. \tag{5}$$

Optimization is terminated when the following conditions are simultaneously satisfied for 15 consecutive iterations:

$$\Delta R^{(t)} < \rho_1,\ S_{grad}^{(t)} < \rho_2,\ \left| S_{temp}^{(t)} - S_{temp}^{(t-1)} \right| < \rho_3, \tag{6}$$

where ρ_1, ρ_2, and ρ_3 are empirically set to 1×10^{-6}, 1×10^{-4}, and 5×10^{-5}, respectively. The threshold values were selected empirically to reflect the scale and stabilization behavior of each normalized convergence indicator in the present 4D mouse cardiac MRI dataset. The data-fidelity threshold ρ_1 was used to identify a plateau in the normalized residual, indicating that further optimization produced negligible improvement in matching the degraded observation. The gradient-stabilization threshold ρ_2 was chosen to ensure that edge-related structures had become stable while avoiding prolonged optimization that may amplify noise-like high-frequency components. The temporal-consistency threshold ρ_3 was selected to confirm that the frame-to-frame variation across cine phases had reached a stable regime. Because Adam-based DIP optimization can exhibit small transient oscillations, the stopping conditions were required to be satisfied for 15 consecutive iterations. This consecutive-iteration rule was introduced to reduce the likelihood of premature stopping caused by short-term numerical fluctuations and to ensure sustained convergence across data fidelity, structural stability, and temporal consistency. Although these parameters provided stable behavior in the present experiments, they should be regarded as empirically determined values and may require recalibration for different imaging protocols, noise levels, or degradation models. This stopping strategy enables sufficient recovery of high-frequency structures required for super-resolution while preventing overfitting to noise, resulting in a balanced reconstruction suitable for 4D MRI applications.

2.3. Quantitative evaluation of image quality

To evaluate the noise level, the contrast-to-noise ratio (CNR) was used. CNR was calculated by placing regions of interest (ROIs) on the mouse image of a representative subject and extracting individual values, from which the mean was computed. For CNR evaluation, regions of interest (ROIs) were selected within the cardiac region of the mouse and in an appropriate background area. The CNR was defined as follows [22]:

$$CNR = \frac{|S_T - S_{BK}|}{\sqrt{\sigma_T^2 + \sigma_{BK}^2}}, \tag{7}$$

where S_T and S_{BK} denote the mean signal intensities in the target and background regions, respectively; σ_T and σ_{BK} denote the corresponding standard deviations.

To assess the level of deblurring in the reconstructed MR image, the gradient magnitude (GM) and perceptual sharpness index (PSI) were employed as evaluation metrics. GM and PSI were computed for all 130 mouse cardiac MR image datasets, and their means and standard deviations were reported. GM and PSI indicate superior image restoration capabilities as their values increase and decrease, respectively. GM quantifies edges and structural variations within an image. Common gradient operators include Sobel, Prewitt, and Scharr. In medical image analysis, GM relies on the principle that pixel intensity reflects underlying tissue characteristics and is computed from intensity gradients in both horizontal and vertical directions [23]. The general formulation of GM using these three gradient operators is given as follows [24]:

$$GM = \sqrt{G_x^2 + G_y^2}, \tag{8}$$

where G_x and G_y represent the gradients in the horizontal and vertical directions, respectively. Additionally, the PSI was employed to quantitatively assess the perceived image sharpness [25]. As an evaluation metric designed to reflect characteristics of the human visual system, PSI enables a comprehensive evaluation of both gradient information and noise in MR images.

3. Results and Discussion

Figure 2 presents representative coronal sections from 4D cardiac MR images of a mouse. Fig. 2(a) shows the degraded image, which exhibits substantial noise and blurring across the entire region, including the heart. Fig. 2(b) presents the result of applying a combined block-matching and 4D filtering (BM4D) [26] and total generalized variation (TGV) algorithm [27] to the degraded image. Relative to Fig. 2(a), this approach reduces noise and yields modest improvement in the visualization of cardiac structures. Fig. 2(c) shows the result of applying the proposed method to the degraded image, which achieves a more substantial reduction in noise, along with noticeably less blurring than Fig. 2(b).

Overall, the proposed method provides improved visualization of cardiac anatomy in 4D mouse cardiac MR images. Internal structures, including the ventricles and blood-filled regions, are more clearly delineated. The bright elliptical structure at the center of the left ventricle is distinctly visible. In addition, boundaries between the myocardium and blood in both ventricles, along with fine structural details, are well preserved, and the connections of major vessels are more clearly defined.

Figure 3 presents the graph of CNR values calculated using the ROIs indicated in Fig. 2. The mean CNR values

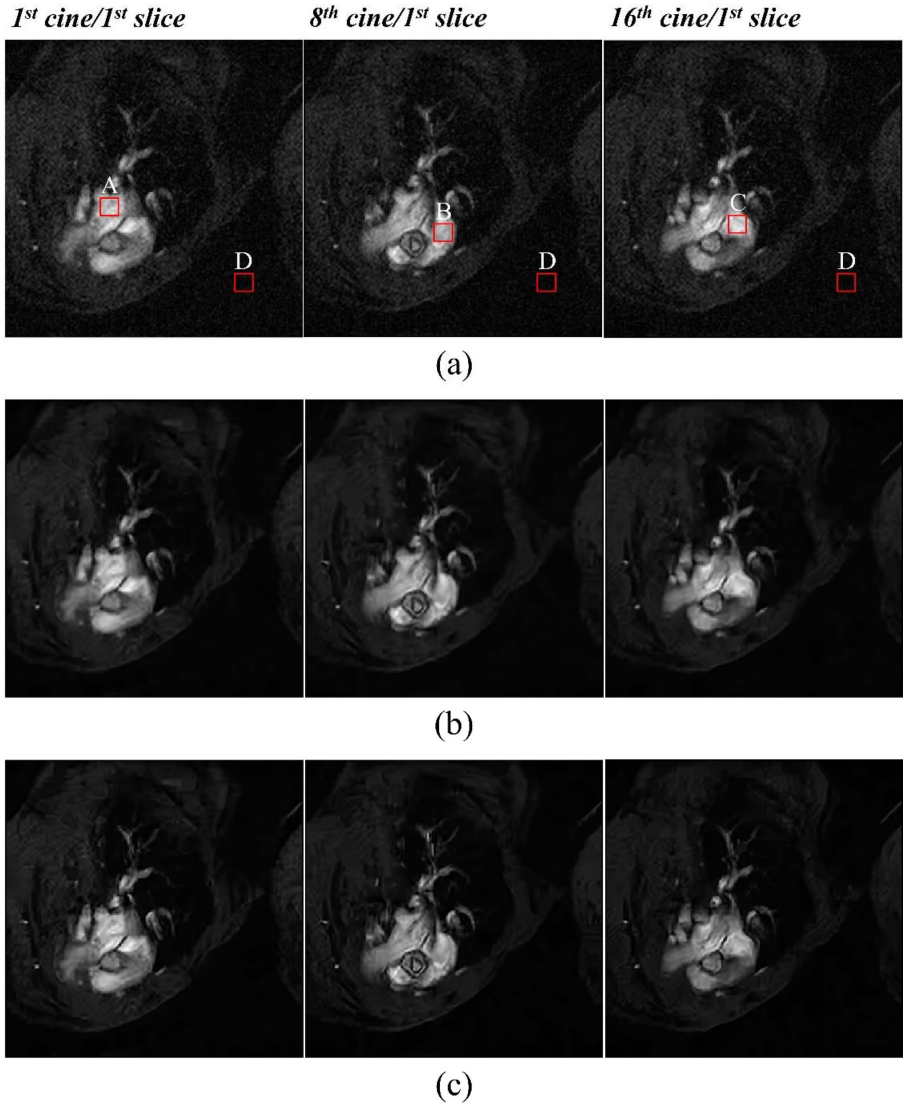

Fig. 2. (Color online) Coronal slices of mouse cardiac MR images (cine frames 1, 8, and 16 from the first slice): (a) degraded images with regions of interests (ROIs) indicated for quantitative analysis; (b) images processed using the block-matching and 4D filtering (BM4D) combined with total generalized variation (TGV); and (c) images processed using the proposed method.

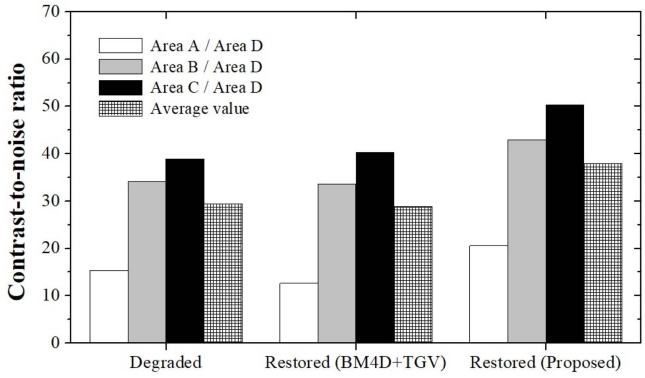

Fig. 3. Quantitative comparison of contrast-to-noise ratio (CNR) based on the ROIs shown in Figure 2. The proposed method achieves the highest mean CNR across all regions when applied to degraded images.

across three measurements were 29.49 for the degraded image, 28.83 for the image processed using the BM4D–TGV method, and 37.95 for the MR image processed with the proposed method. Compared to the BM4D–TGV approach, the proposed method achieved an approximate 31.63% improvement in CNR.

Figure 4(a) and (b) illustrate the graphs of the computed GM and PSI values, respectively. For 130 cases, the GM values (mean ± standard deviation) were 59.04 ± 8.83 for the degraded image, 226.26 ± 32.67 after BM4D–TGV processing, and 558.35 ± 32.52 for the proposed method. Compared with the application of the BM4D and TGV fusion method to the degraded image, the proposed method demonstrated an approximate 146.77% improvement in GM. The PSI values (mean ± standard deviation) were 0.600 ± 0.028 for the degraded image, 0.380 ± 0.030 after BM4D–TGV processing, and 0.140 ± 0.021 for the proposed method. Compared with the application of the BM4D and TGV fusion method to the degraded image, the proposed method yielded an approximate 63.16% improvement in PSI.

This study demonstrates that a DIP-based approach, which does not require external training data, can effectively enhance the image quality of mouse cardiac MRI. The proposed method improves structural clarity and contrast, even under low signal-to-noise ratio conditions, while the hybrid stopping strategy mitigates noise overfitting during reconstruction. These findings highlight the potential of data-efficient, self-supervised reconstruction techniques as a powerful alternative in small-animal imaging, where acquiring large-scale training datasets is inherently challenging.

DIP demonstrates strong potential for application to 4D MRI, where motion is prominent and high temporal

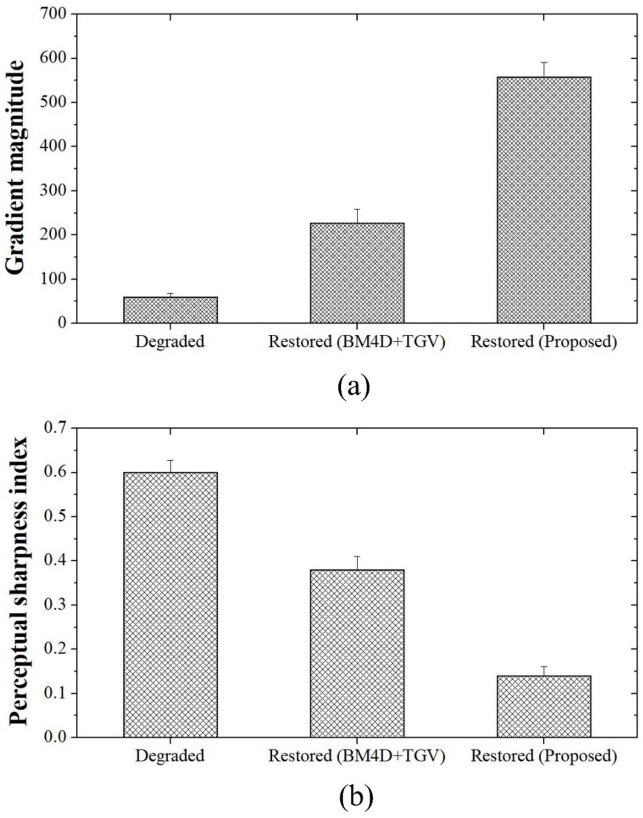

Fig. 4. Quantitative comparison of (a) gradient magnitude (GM) and (b) perceptual sharpness index (PSI) computed from 130 mouse cardiac MR image datasets. The proposed method yields the highest GM and PSI values when applied to cardiac MR images.

resolution is critical. Yoo *et al.* extended DIP to dynamic MRI by modeling temporal information using a low-dimensional manifold [28]. Building upon this concept, the present study further refines the approach by incorporating super-resolution and denoising strategies into the conventional DIP framework. In addition, data consistency was effectively integrated into the reconstruction process, enabling successful application to cardiac MR images. Future work will extend the proposed algorithm to human MRI datasets involving highly dynamic organs to evaluate its feasibility and potential for clinical translation.

Although this study focused on cardiac MRI, the proposed DIP framework is potentially applicable to various medical imaging modalities. This approach may be especially useful for brain MRI and computed tomography (CT) imaging of neurodegenerative diseases, such as Alzheimer's disease, where subtle anatomical alterations, including cortical atrophy and hippocampal volume loss, play an important role in diagnosis and disease progression assessment [29, 30]. In addition, the framework

may have significant clinical value in low-dose imaging applications, such as pediatric X-ray radiography and CT, by enhancing image quality without increasing radiation exposure. These potential applications highlight the broader clinical utility and translational potential of the proposed approach.

The proposed method has several limitations. A primary limitation is its reliance on a predefined degradation model. In this study, the forward operator was modeled using Gaussian blurring and uniform downsampling combined with additive Gaussian noise. Although this formulation provides a convenient and mathematically tractable approximation, it does not fully capture the complex physical processes underlying MRI acquisition, such as k-space undersampling, coil sensitivity variation, and non-Gaussian noise characteristics. Consequently, reconstruction performance may be suboptimal when applied to real-world MRI data that deviates from the assumed degradation model [31]. This limitation is inherent to model-based self-supervised reconstruction approaches and suggests that future work should incorporate more realistic forward models, potentially integrating physics-informed operators or scanner-specific acquisition modeling to improve generalizability.

The threshold values and the 15-consecutive-iteration window remain empirically determined. These parameters were designed to capture the stabilization of data consistency, gradient-domain structure, and temporal coherence in the present dataset, but they do not provide a theoretical guarantee of optimal stopping. This is particularly important for DIP-based reconstruction, where the implicit regularization effect depends strongly on the optimization trajectory and iteration number. Therefore, future work should include sensitivity analyses across threshold values, adaptive stopping rules based on validation-free uncertainty estimation, or discrepancy-principle-based stopping criteria when noise statistics are known. Furthermore, DIP-based methods exhibit implicit regularization behavior that depends strongly on optimization dynamics, making them sensitive to early stopping [32]. Despite the improved robustness of the proposed hybrid strategy relative to conventional frequency-based stopping methods, the risk of premature termination or delayed stopping persists. Future studies should investigate adaptive or theoretically grounded stopping mechanisms to further enhance stability and reliability.

4. Conclusion

A DIP-based approach can effectively enhance image quality in mouse cardiac MRI. The proposed method improves structural clarity and contrast while mitigating noise overfitting through a hybrid stopping strategy. These findings highlight the potential of self-supervised reconstruction techniques for small-animal imaging and support their future extension to more complex and clinically relevant MRI applications.

Acknowledgment

We thank the J. Steeden Research Group, University College London, for providing the data used in this study.

Funding

This work was supported by the National Research Foundation of Korea (NRF) grant funded by the Korea government (MSIT) (RS-2026-25469485).

References

[1] S.-E. Lee, C. Nguyen, Y. Xie, Z. Deng, Z. Zhou, D. Li, and H.-J. Chang, Korean Circulation Journal **49**, 146 (2019).

[2] P. S. Rajiah, C. J. Francois, and T. Leiner, Radiology **307**, e223008 (2023).

[3] M. Stuber, R. M. Botnar, S. E. Fischer, R. Lamerichs, J. Smink, P. Harvey, and W. J. Manning, Magnetics Resonance in Medicine **48**, 425 (2002).

[4] A. N. Price, K. K. Cheung, J. O. Cleary, A. E. Campbell, J. Riegler, and M. F. Lythgoe, The Open Cardiovascular Medicine Journal **4**, 278 (2010).

[5] A. Akki, A. Gupta, and R. G. Weiss, American Journal of Physiology - Heart and Circulatory Physiology **304**, H633 (2013).

[6] H. Li, P. Metze, A. Abaei, W. Rottbauer, S. Just, Q. Lu, and V. Rasche, NMR in Biomedicine **33**, e4300 (2020).

[7] N. Jiang, Y. Zhang, Q. Li, X. Fu, and D. Fang, Physics in Medicine and Biology **69**, 095004 (2024).

[8] E. van Reeth, I. W. K. Tham, C. H. Tan, and C. L. Poh, Concepts in Magnetic Resonance: Part A **40A**, 306 (2012).

[9] O. N. Jaspan, R. Fleysher, and M. L. Lipton, British Journal of Radiology **88**, 20150487 (2015).

[10] R. R. Upendra, R. Simon, and C. A. Linte, 2021 Computing in Cardiology (2022) DOI: 10.23919/CinC53138.2021.9662790.

[11] D. Ulyanov, A. Vedaldi, and V. Lempitsky, Proceedings of the IEEE Conference on Computer Vision and Pattern Recognition (CVPR), **9446** (2018).

[12] M. A. Sultan, C. Chen, Y. Liu, K. Gil, K. Zareba, and R. Ahmad, Magnetic Resonance Materials in Physics, Biology and Medicine **38**, 859 (2025).

[13] M. Vornehm, C. Chen, M. A. Sultan, S. M. Arshad, Y. Han, F. Knoll, and R. Ahmad, Magnetic Resonance in Medicine **94**, 2668 (2025).

[14] S.-H. Kang, K. Kim, J. Shim, and Y. Lee, Scientific Reports **15**, 13281 (2025).
[15] W. Shah, D. J. Stuckey, T. Yao, M. Wrobel, E. Deniszczyc, Z. Feng, S. Anderson, R. Campbell, V. Muthurangu, and J. Steeden, Journal of Cardiovascular Magnetic Resonance, **28**, 102706 (2026).
[16] K. Zhang, W. Zuo, Y. Chen, D. Meng, and L. Zhang, IEEE Transactions on Image Processing **26**, 3142 (2017).
[17] C. Dong, C. C. Loy, K. He, and X. Tang, IEEE Transactions on Pattern Analysis and Machine Intelligence **38**, 295 (2016).
[18] A. L. Aswathy and S. S. Vinod Chandra, Scientific Reports **12**, 3090 (2022).
[19] L. I. Rudin, S. Osher, and E. Fatemi, Physica D **60**, 259 (1992).
[20] R. Otazo, E. Candès, and D. K. Sodickson, Magnetic Resonance in Medicine **73**, 1125 (2015).
[21] J. Yao, Z. Xu, X. Huang, and J. Huang, Medical Image Analysis **44**, 14 (2018).
[22] K. Kim and Y. Lee, Radiation Physics and Chemistry **245**, 113862 (2026).
[23] K. Kim and Y. Lee, Electronics **14**, 743 (2025).
[24] L. Zhang, L. Zhang, X. Mou, and D. Zhang, IEEE Transactions on Image Processing **20**, 2378 (2011).
[25] C. Feichtenhofer, H. Fassold, and P. Schallauer, IEEE Signal Processing Letters **20**, 379 (2013).
[26] R. Ayde, G. Zihlmann, N. Salameh, and M. Sarracanie, Magnetic Resonance Materials in Physics, Biology and Medicine (2025).
[27] S. Wali, H. Zhang, H. Chang, and C. Wu, Journal of Visual Communication and Image Representation **59**, 39 (2019).
[28] J. Yoo, K. H. Jin, H. Gupta, J. Yerly, M. Stuber, and M. Unser, IEEE Transactions on Medical Imaging **40**, 3337 (2021).
[29] S. Lim and Y. Lee, Medical Physics **53**, e70379 (2026).
[30] S. Lim, H. Kim, and Y. Lee, PLoS One **20**, e0329893 (2025).
[31] M. Lustig, D. Donoho, and J. M. Pauly, Magnetic Resonance in Medicine **58**, 1182 (2007).
[32] V. Lempitsky, A. Vedaldi, and D. Ulyanov, 2018 IEEE/CVF Conference on Computer Vision and Pattern Recognition, 9446 (2018).